Supporting Information

Defective Transition Metal Hydroxide Based Nanoagent with Hypoxia Relief for Photothermal-enhanced Photodynamic Therapy

Tianren Xu,[a] Xiaojiao Zhu,[*a] Li Yang,[a] Yingcui Bu,[a] Yuyang Zhang,[a] Jie Zhang,[b] Lianke Wang,[b] Zhipeng Yu[b] and Hongping Zhou[*a]

[a] College of Chemistry and Chemical Engineering, Anhui University and Key Laboratory of Functional Inorganic Materials Chemistry of Anhui Province, Anhui Province Key Laboratory of Chemistry for Inorganic/Organic Hybrid Functionalized Materials, Key Laboratory of Structure and Functional Regulation of Hybrid Materials (Anhui University) Ministry of Education, Hefei, 230601, P. R. China.

[b] Institute of Physical Science and Information Technology, Faculty of Health Sciences, Anhui University, Hefei, 230601, P. R. China.

[*] Corresponding authors: xiaojzhu@ahu.edu.cn (Xiaojiao Zhu) and zhpzhp@263.net (Hongping Zhou).

Supporting Information

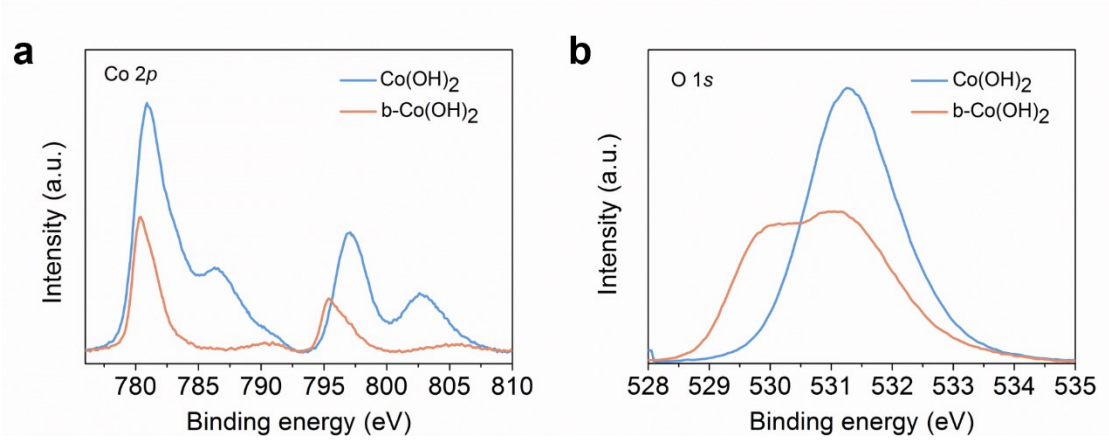

Fig. S1. (a) Co 2p XPS spectra of $Co(OH)_2$ and b-$Co(OH)_2$. (b) O 1s XPS spectra of $Co(OH)_2$ and b-$Co(OH)_2$.

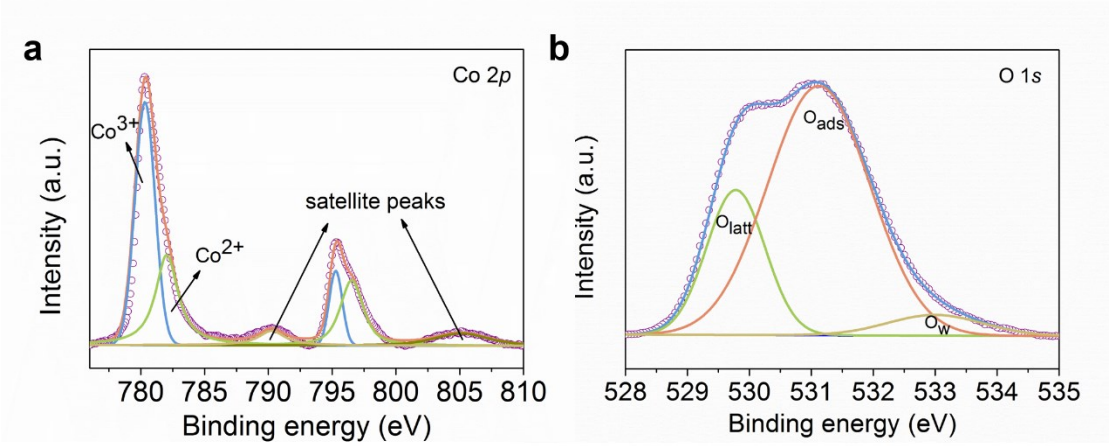

Fig. S2. (a) XPS Co 2p spectra of b-$Co(OH)_2$. (b) XPS O 1s spectra of b-$Co(OH)_2$.

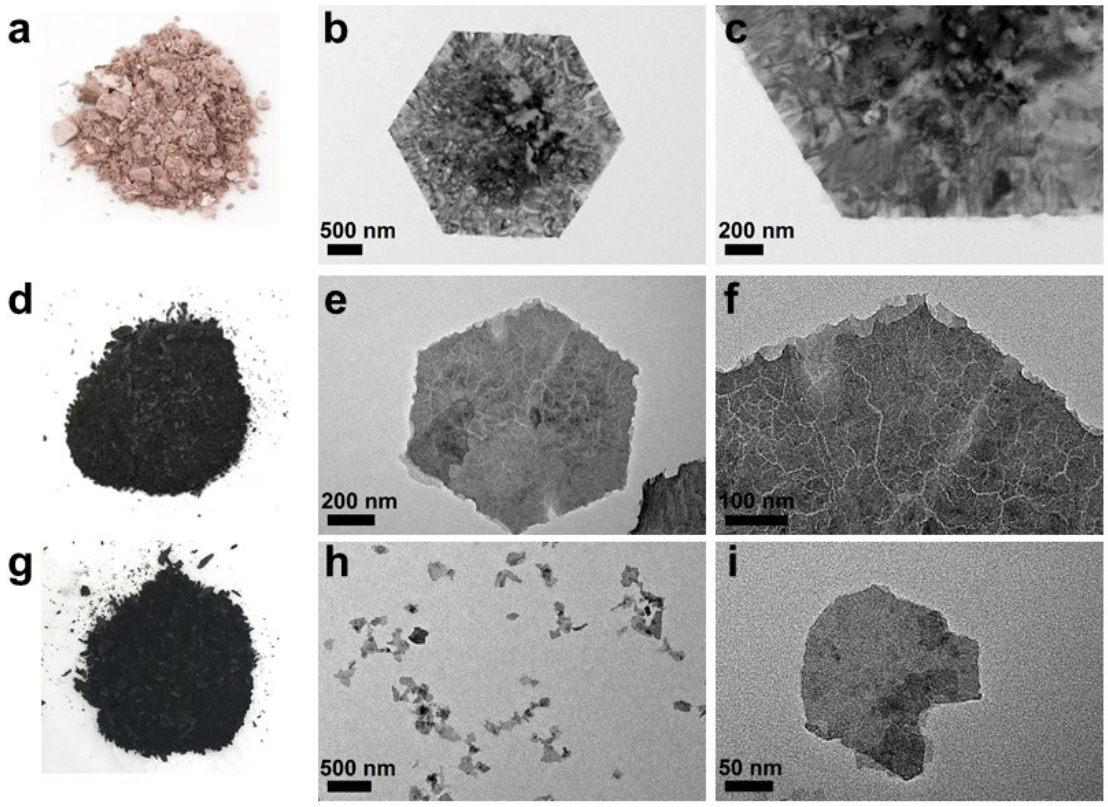

Fig. S3. Digital pictures of (a) Co-Ni hydroxides, (d) b-Co-Ni hydroxides and (g) b-Co-Ni hydroxides (after tip-sonication) powder. TEM images of (b-c) Co-Ni hydroxides, (e-f) b-Co-Ni hydroxides and (h-i) b-Co-Ni hydroxides (after tip-sonication) nanosheets at different scales.

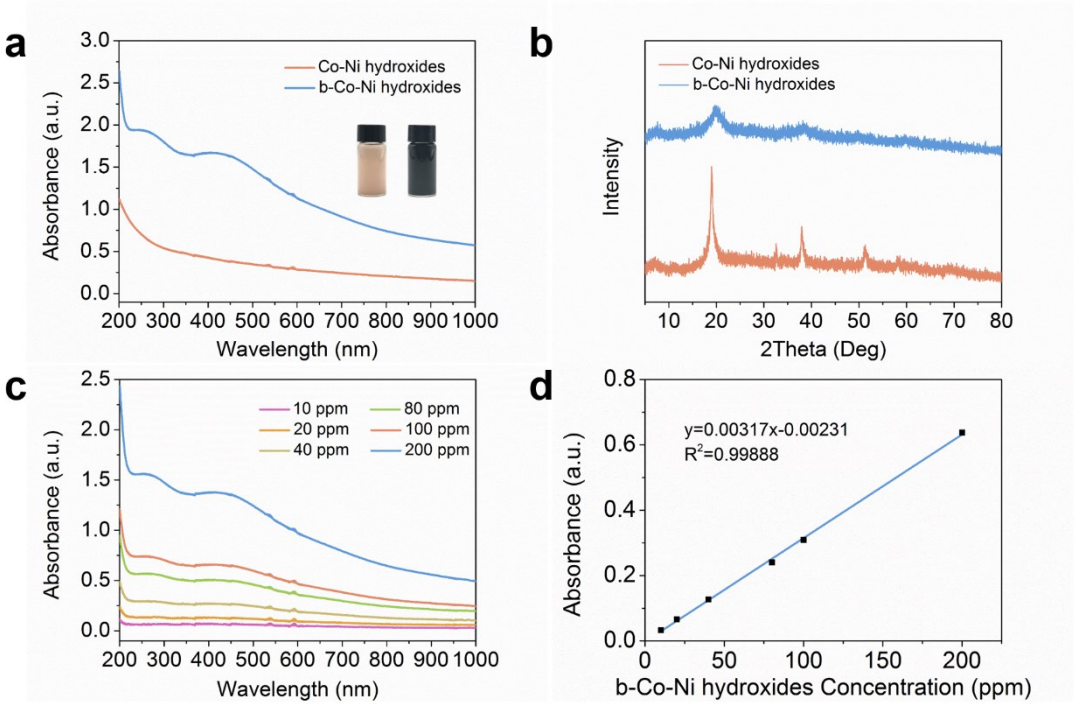

Fig. S4. (a) UV-vis spectra of Co-Ni hydroxides and b-Co-Ni hydroxides. The inset showed the color change of Co-Ni hydroxides after oxidation. (b) XRD patterns of Co-Ni hydroxides and b-Co-Ni hydroxides. (c) UV-vis spectra of b-Co-Ni hydroxides at different concentrations. (d) The linear relationship between optical absorbance and the concentration of b-Co-Ni hydroxides at 808 nm.

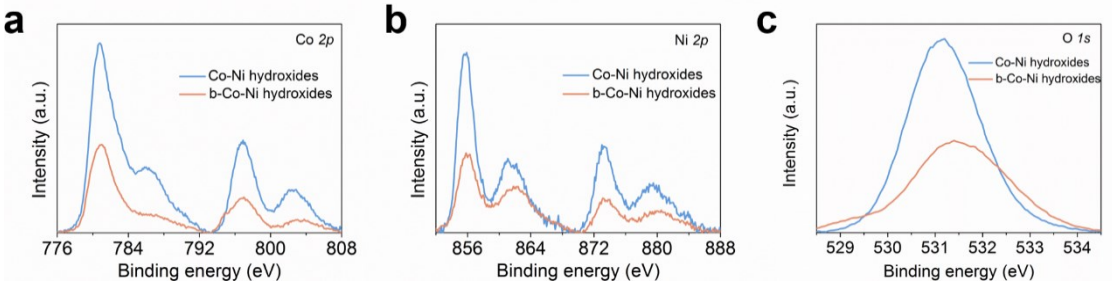

Fig. S5. (a) Co 2p XPS spectra of Co-Ni hydroxides and b-Co-Ni

hydroxides. (b) Ni 2p XPS spectra of Co-Ni hydroxides and b-Co-Ni hydroxides. (c) O 1s XPS spectra of Co-Ni hydroxides and b-Co-Ni hydroxides.

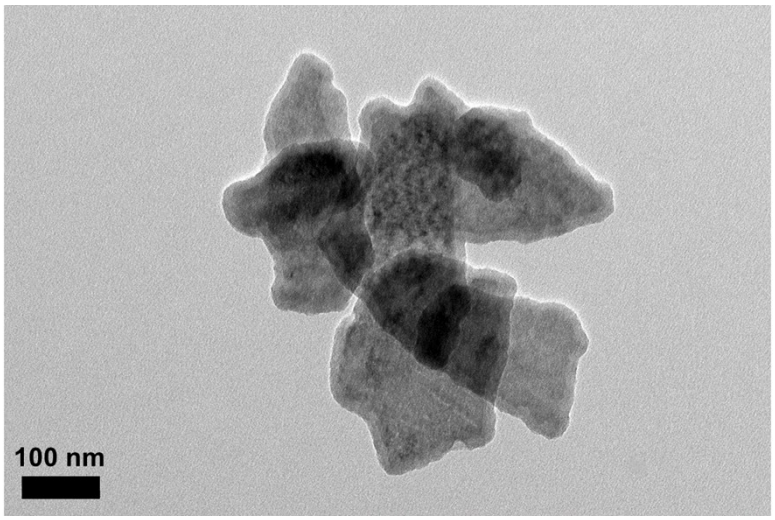

Fig. S6. TEM image of b-$Co(OH)_2$@SiO_2.

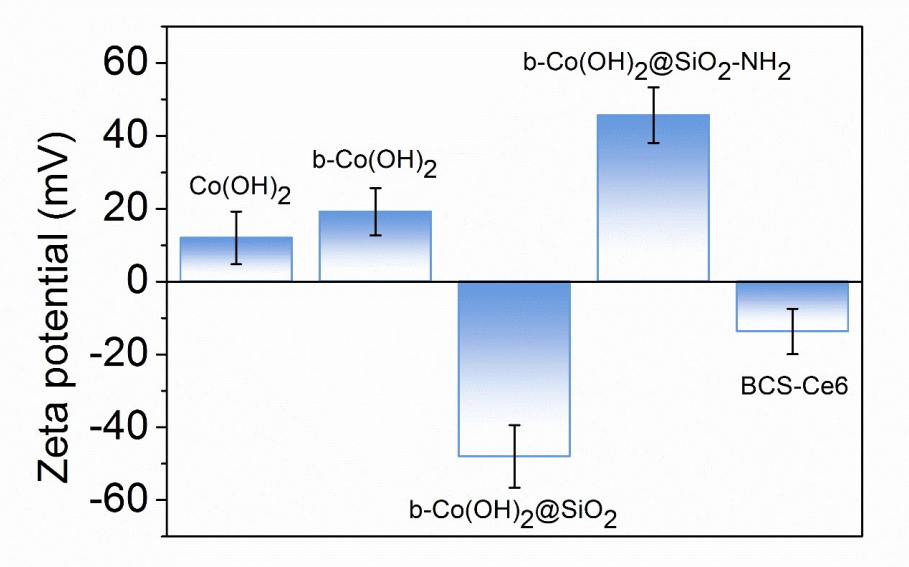

Fig. S7. Zeta potentials of $Co(OH)_2$, b-$Co(OH)_2$, b-$Co(OH)_2$@SiO_2, b-$Co(OH)_2$@SiO_2-NH_2 and BCS-Ce6.

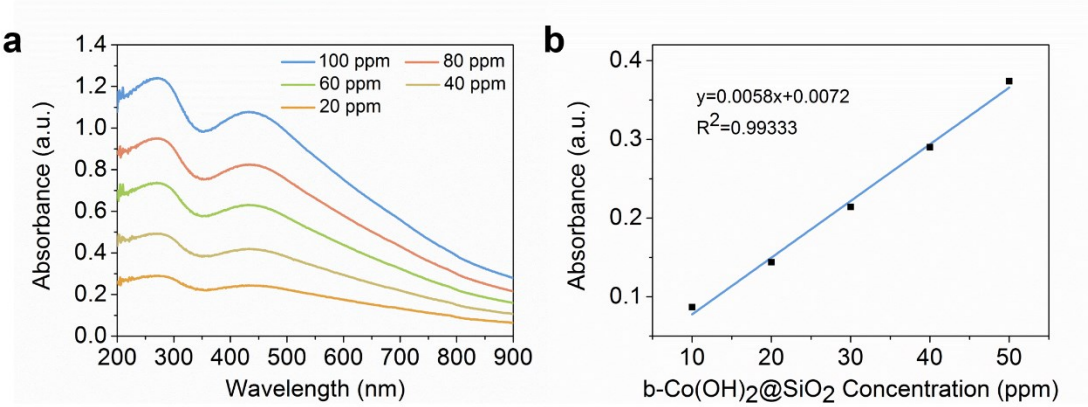

Fig. S8. (a) UV-vis spectra of b-$Co(OH)_2$@SiO_2 at different concentrations. (b) The linear relationship of the absorbance at 808 nm as a function of b-$Co(OH)_2$@SiO_2 concentration.

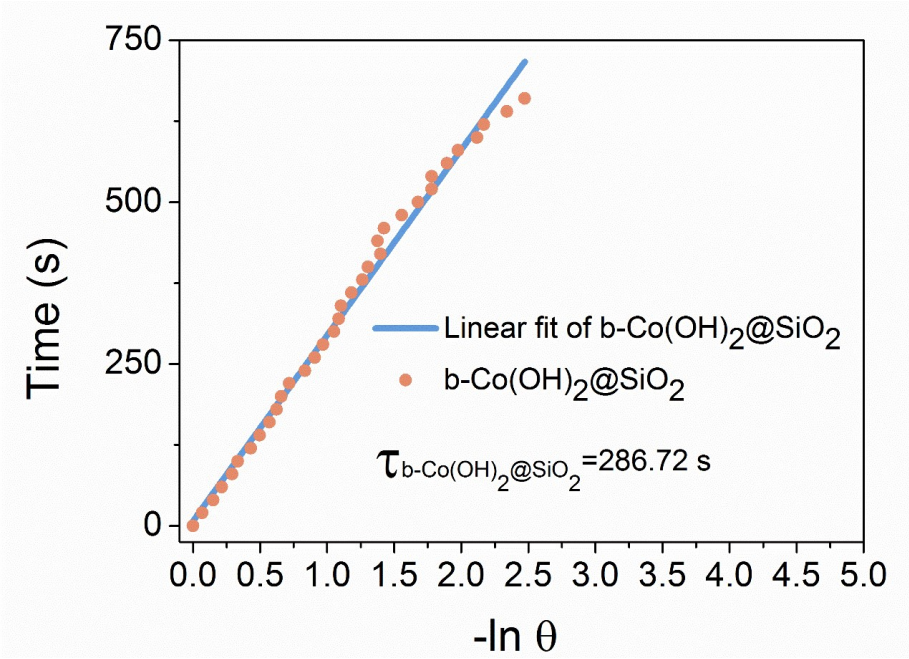

Fig. S9. Linear time data versus –ln θ obtained from the cooling period in Figure 2c of b-$Co(OH)_2$@SiO_2.

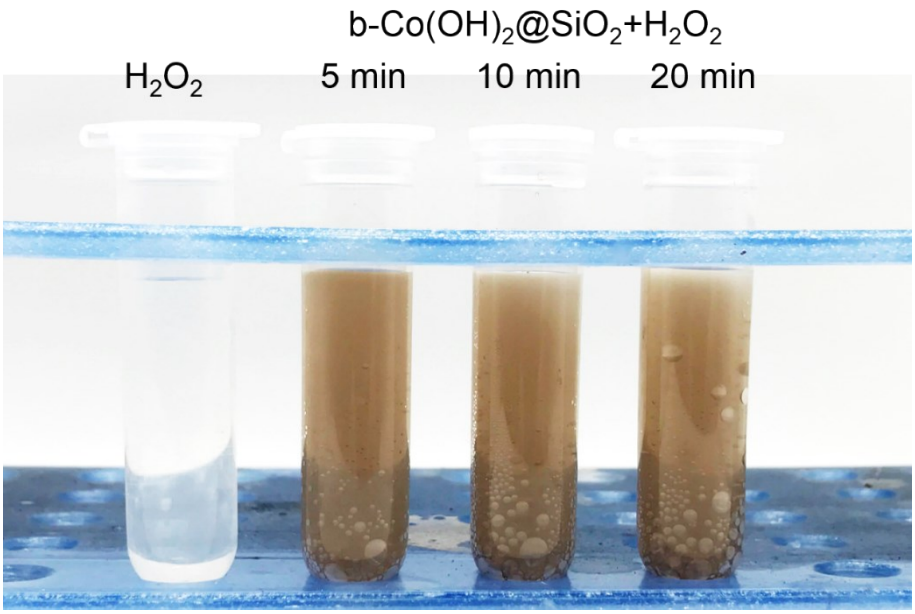

Fig. S10. Pictures of bubbles produced by the decomposition of hydrogen peroxide (5 mM) in the solution of b-$Co(OH)_2$@SiO_2 (100 ppm) at different time points (5 min, 10 min and 20 min).

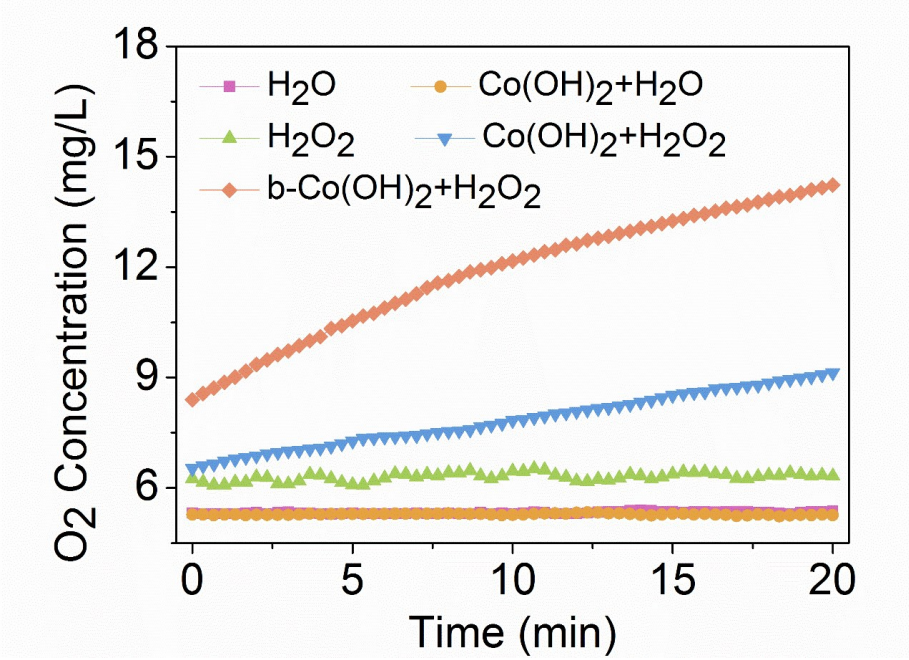

Fig. S11. The oxygen level variation of different solutions (water, H_2O_2, $Co(OH)_2$, $Co(OH)_2$+H_2O_2, b-$Co(OH)_2$+H_2O_2) over time.

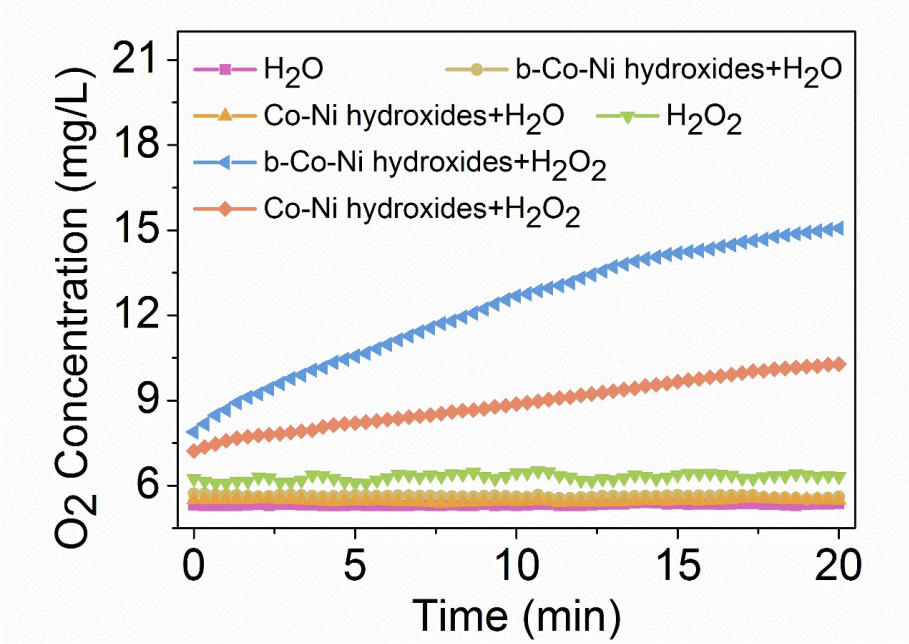

Fig. S12. The oxygen level variation of different solutions (water, H_2O_2, Co-Ni hydroxides, b-Co-Ni hydroxides, Co-Ni hydroxides+H_2O_2 and b-Co-Ni hydroxides+H_2O_2) over time.

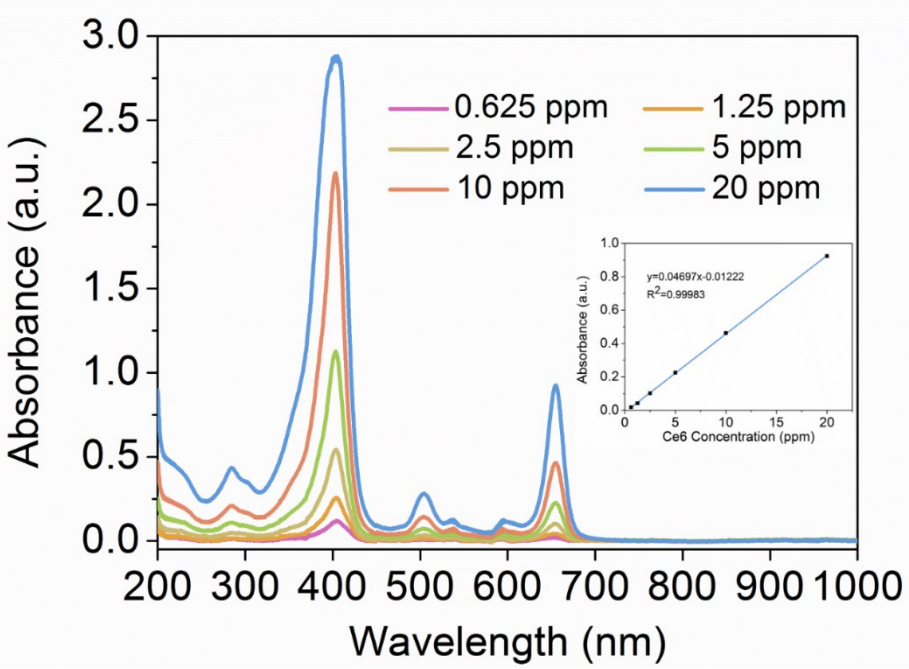

Fig. S13. UV-vis spectra of Ce6 at various concentrations. The inset indicated the normalized absorbance of different Ce6 concentrations at 655

nm.

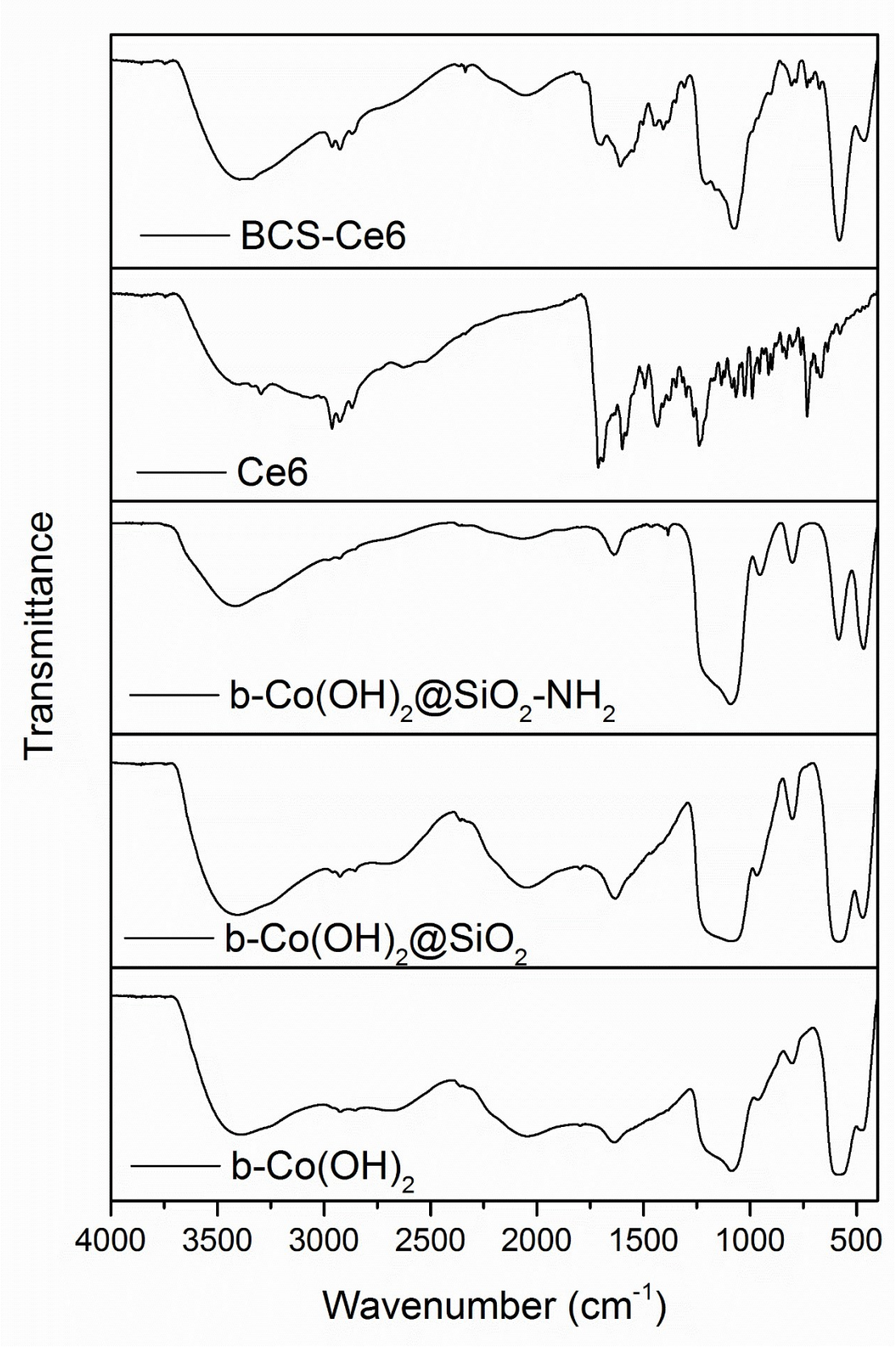

Fig. S14. FT-IR spectroscopy of b-$Co(OH)_2$, b-$Co(OH)_2$@SiO_2, b-

$Co(OH)_2$@SiO_2-NH_2, Ce6 and BCS-Ce6.

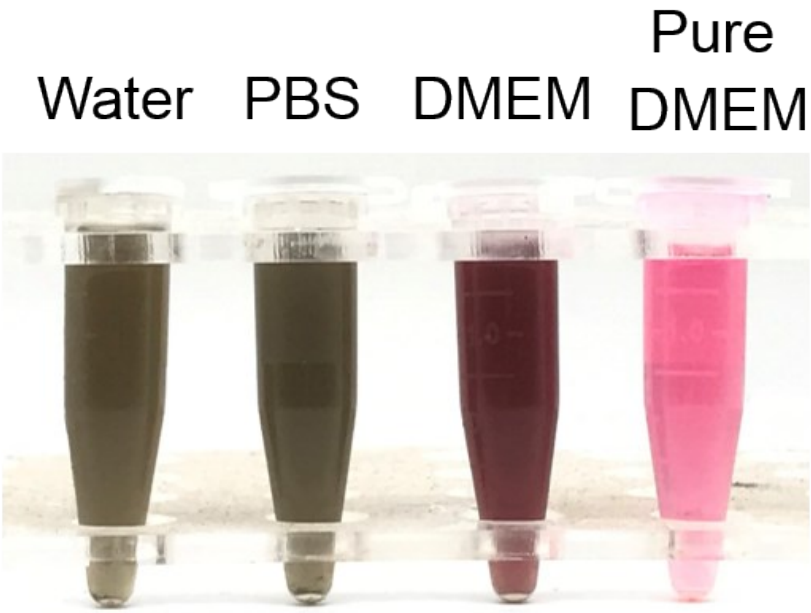

Fig. S15. Photograph of BCS-Ce6 in water, PBS and DMEM. Pure DMEM was placed as a comparison.

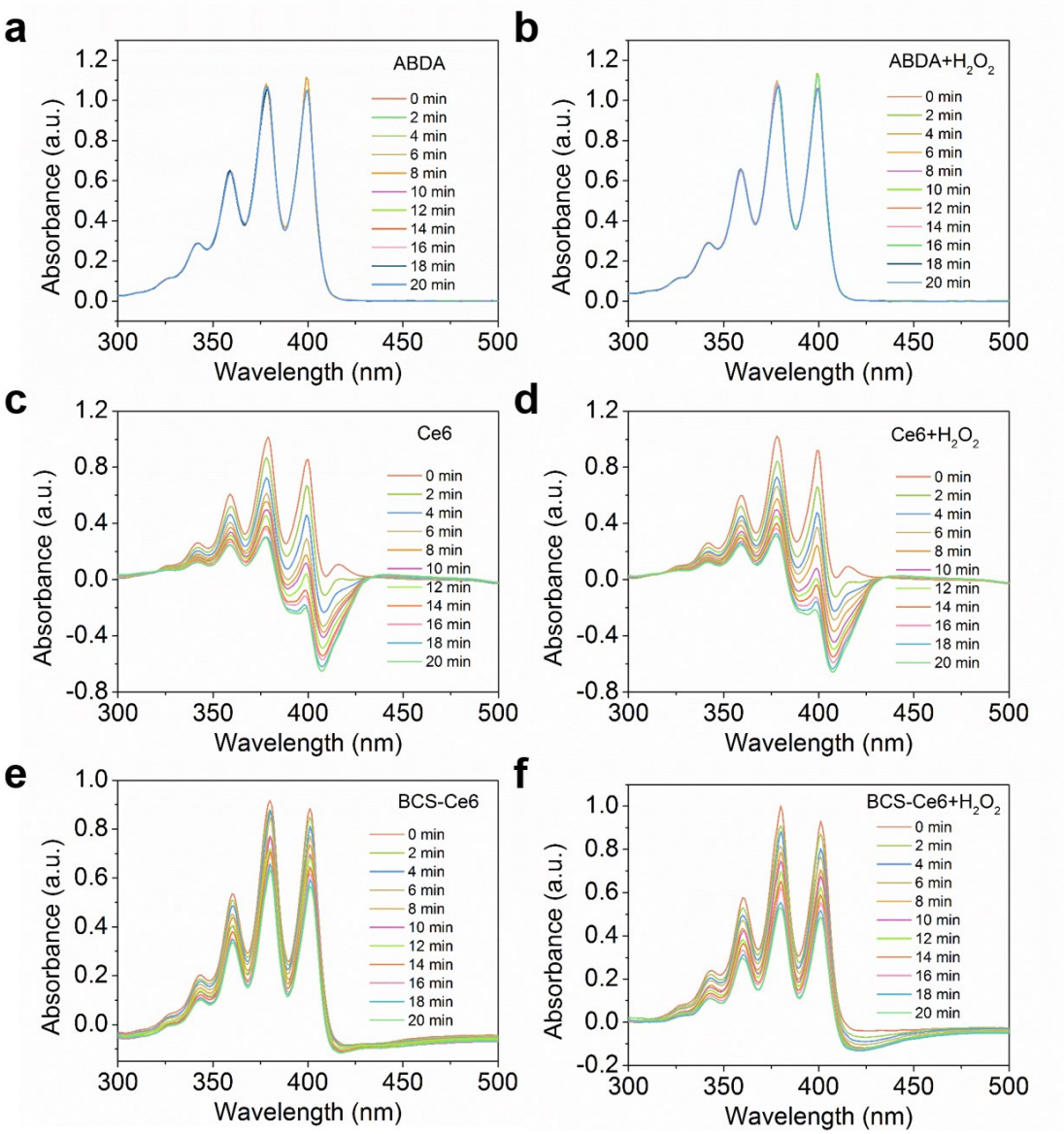

Fig. S16. (a-b) UV-vis spectra variation of ABDA under laser irradiation (660 nm, 0.5 W/cm^2, 20 min) in the absence or presence of hydrogen peroxide (5 mM). (c-d) Absorption spectrum decline of ABDA treated with Ce6 (5 ppm) under laser irradiation (660 nm, 0.5 W/cm^2, 20 min) in the absence or presence of hydrogen peroxide (5 mM). (e-f) UV-vis spectra change of ABDA treated with BCS-Ce6 (50 ppm) under laser irradiation (660 nm, 0.5 W/cm^2, 20 min) with or without the adding of hydrogen

peroxide (5 mM).

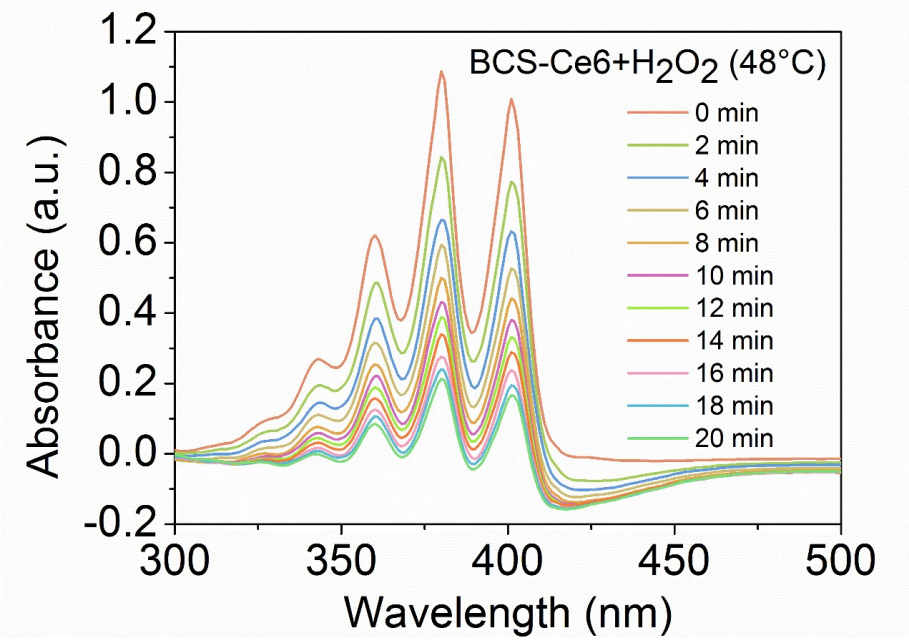

Fig. S17. UV-vis spectra decay of ABDA treated with BCS-Ce6 (50 ppm) and hydrogen peroxide (5 mM) at 48°C under laser irradiation (660 nm, 0.5 W/cm^2, 20 min).

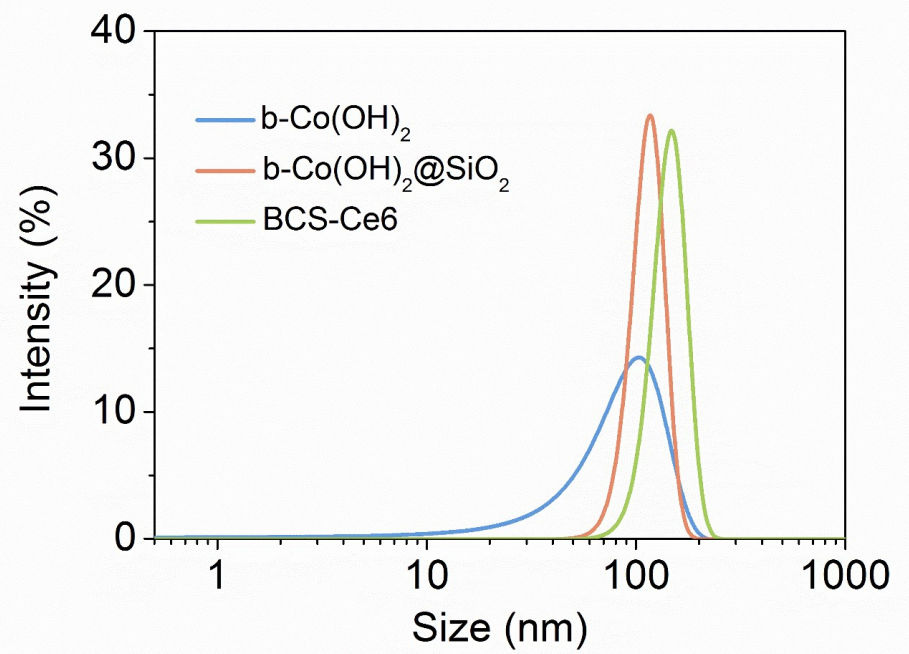

Fig. S18. Size distribution of b-$Co(OH)_2$, b-$Co(OH)_2$@SiO_2 and BCS-Ce6.

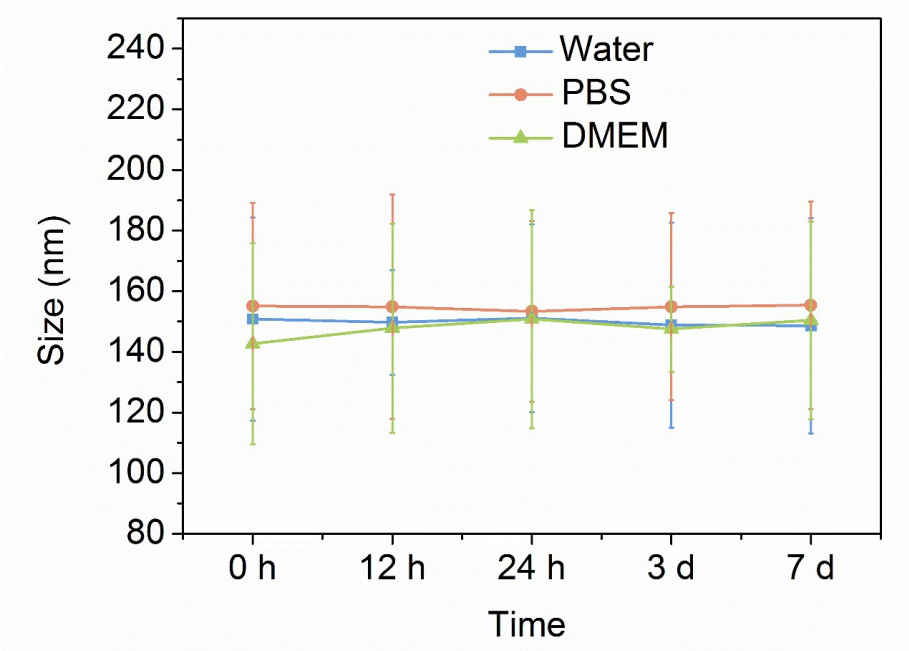

Fig. S19. Size distribution of BCS-Ce6 in various mediums (water, PBS and DMEM) at different time points.

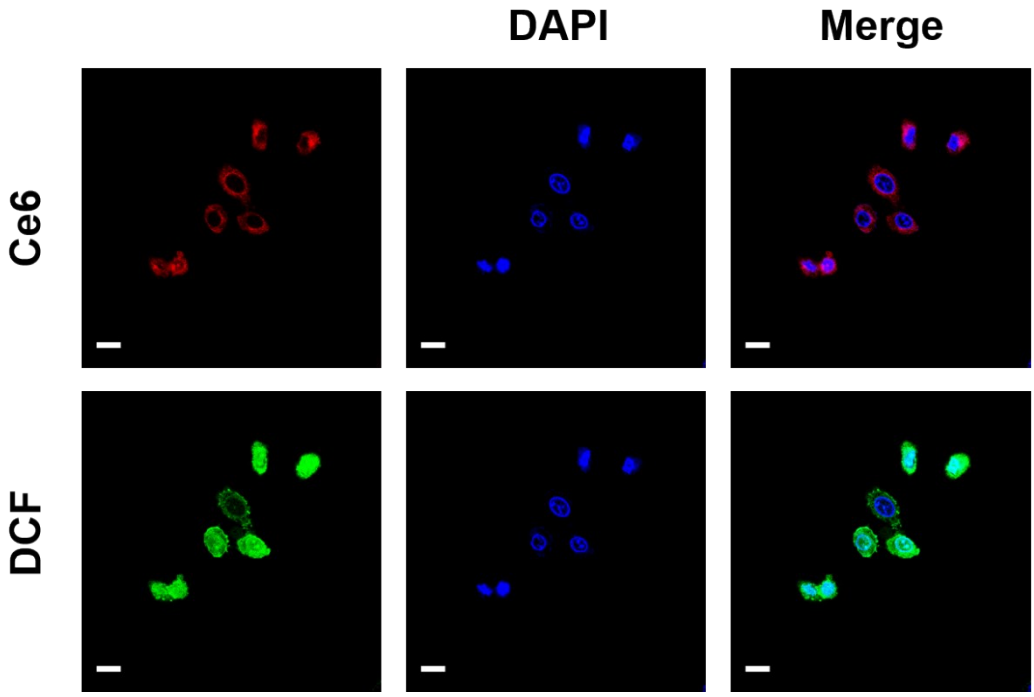

Fig. S20. Intracellular ROS generation detected by DCFH-DA in HepG2 cells incubated with Ce6 under 660 nm laser irradiation. DAPI was used to stain nucleus. Scale bar: 20 μm.

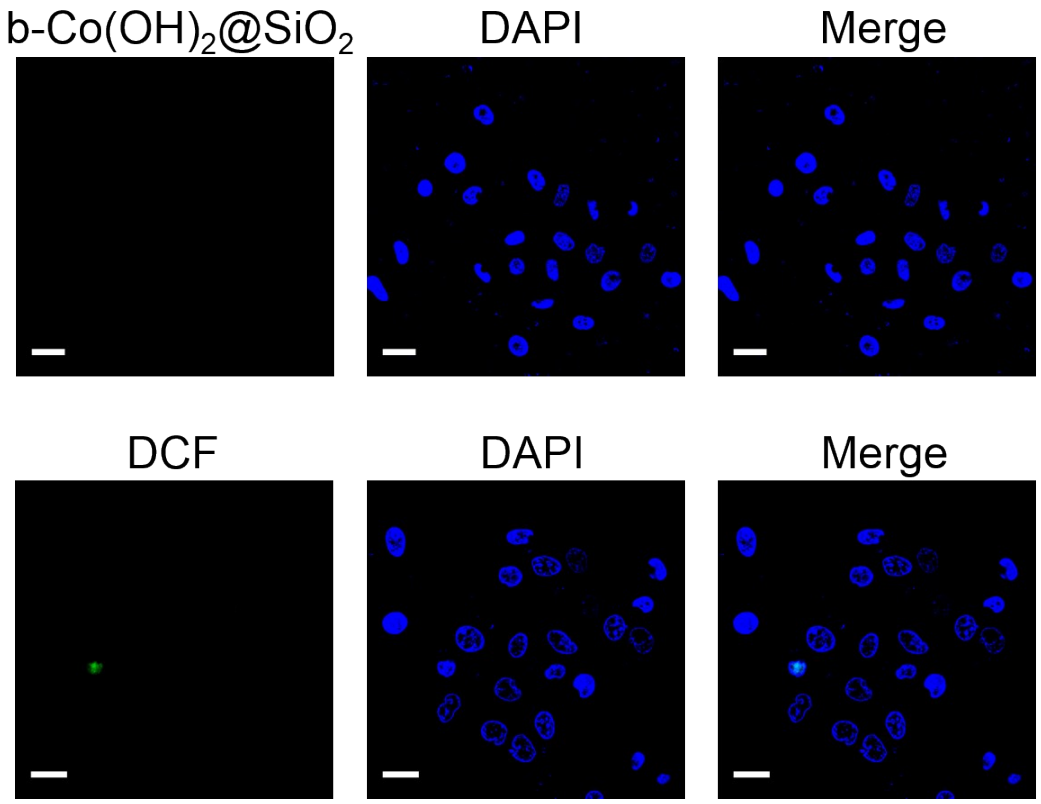

Fig. S21. Florescence imaging of HepG2 cells cultured with b-$Co(OH)_2$@SiO_2 and the detection of intracellular ROS generation in HepG2 cells treated with b-$Co(OH)_2$@SiO_2 upon 660 nm laser irradiation. DAPI was used to locate cells. Scale bar: 20 μm.

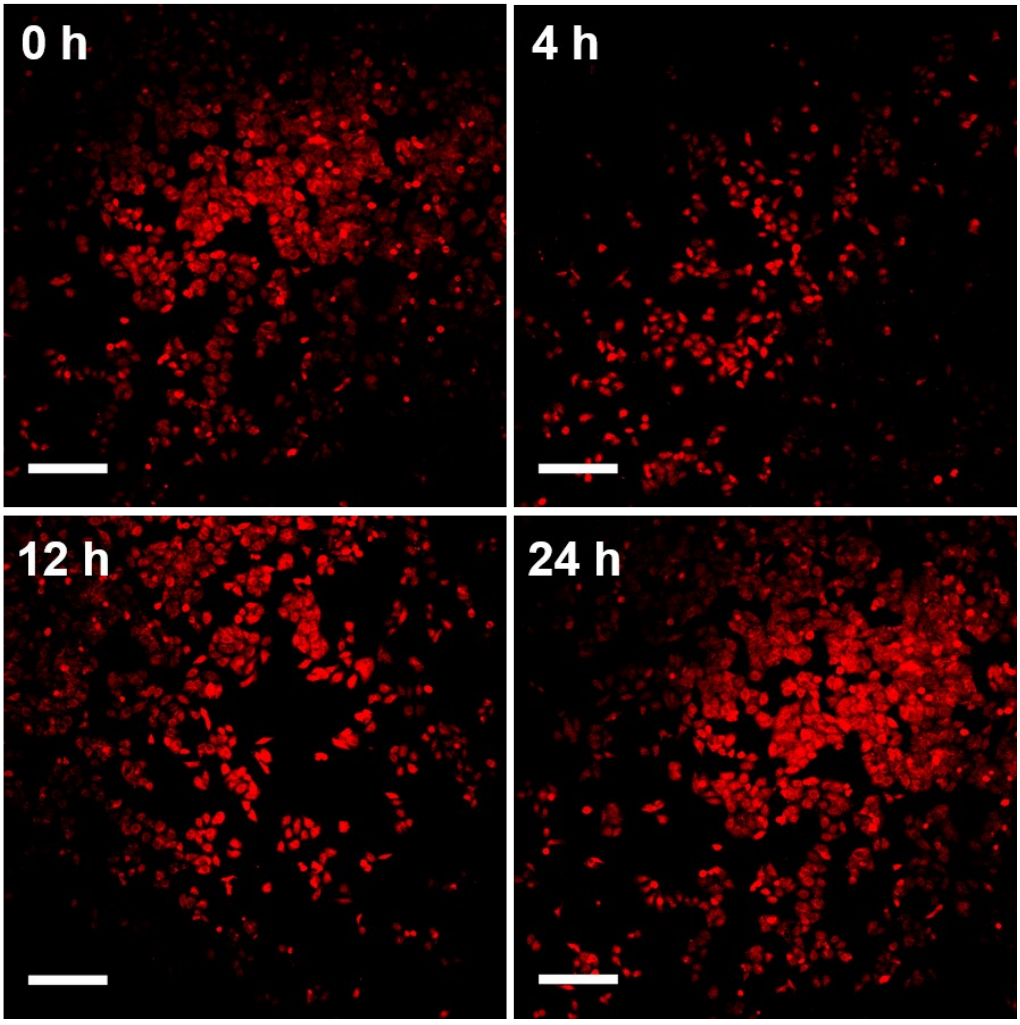

Fig. S22. Intracellular oxygen level monitored by O_2 probe RDPP in HepG2 cells at different time points as a control. Scale bar: 200 μm.

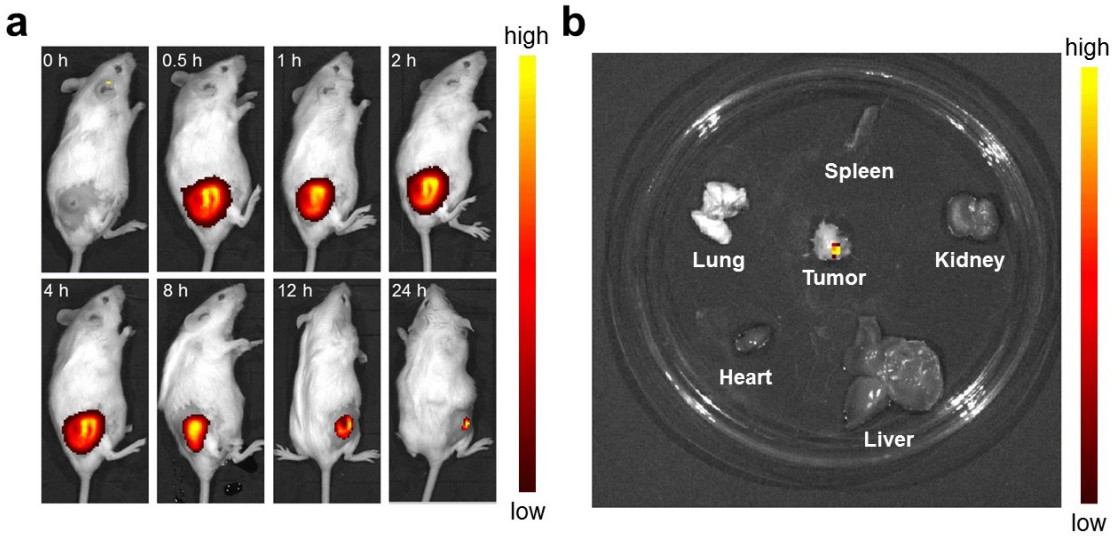

Fig. S23. (a) *In vivo* fluorescence imaging of H22-tumor bearing mice at different points after in-situ injection of Ce6 (500 ppm, 20 μL). (b) Fluorescence images of dissected organs and tumor 24 h after the injection of Ce6.

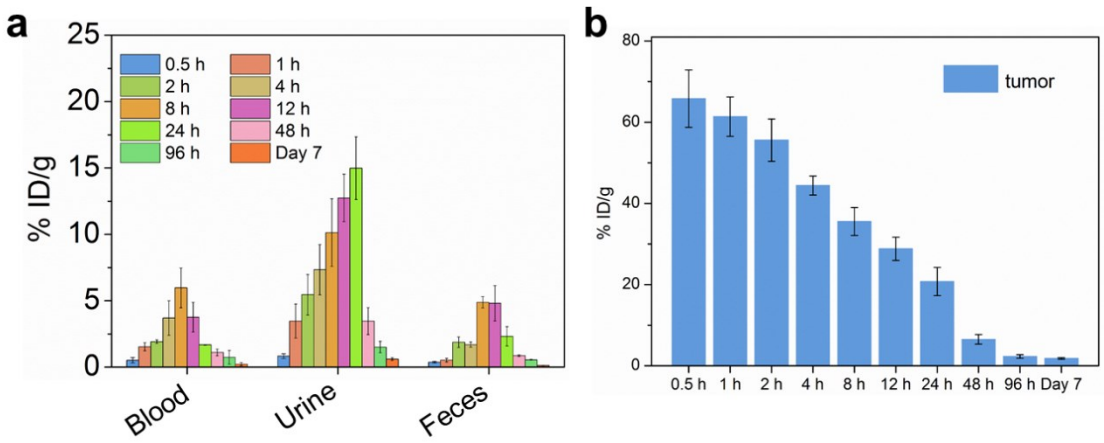

Fig. S24. (a) Biodistribution (blood, urine and feces) of BCS-Ce6 in H22-tumor bearing mice at different time points. (b) Co content at tumor sites over time measured by ICP-MS after the injection of BCS-Ce6. The error bars indicated standard deviations (n=3).

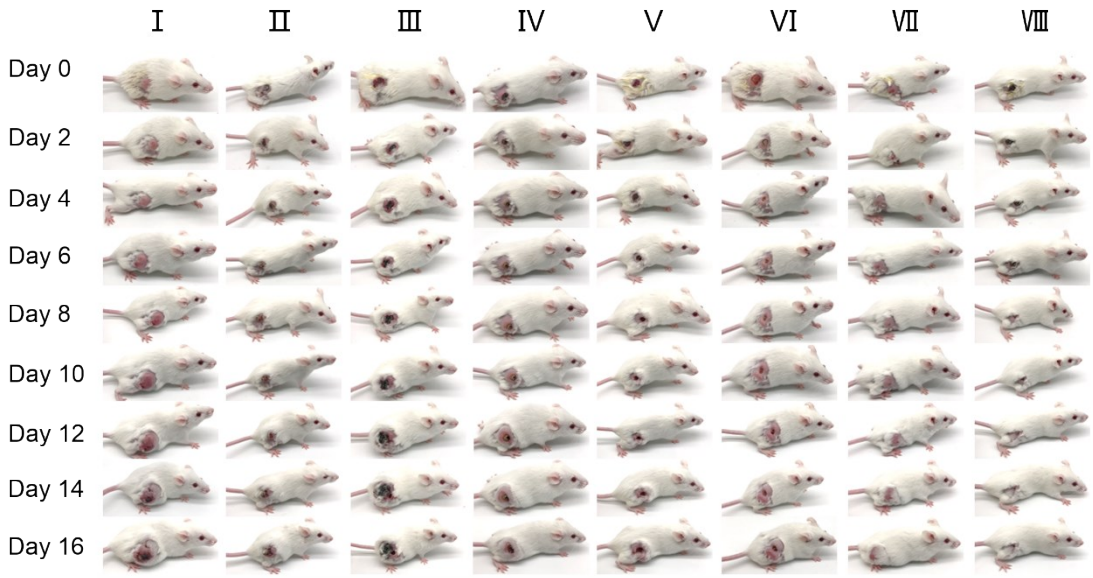

Fig. S25. Representative photos of mice during 16 days with different treatments.

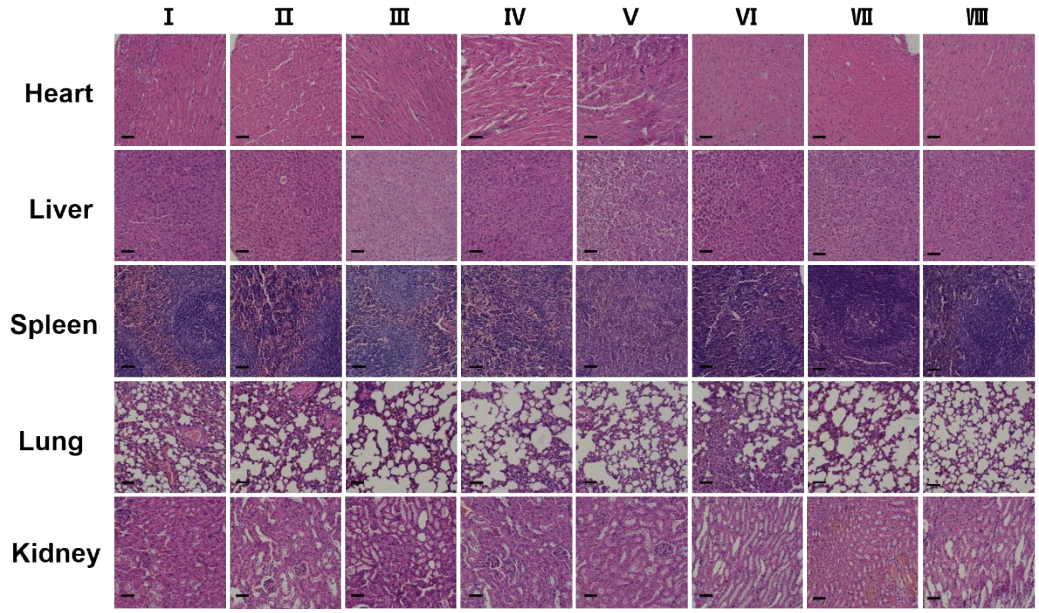

Fig. S26. Hematoxylin and eosin (H&E) staining of main organs dissected from H22-tumor bearing mice 16 days after different treatments. Scale bar: 50 μm.